RSC Advances

PAPER

View Article Online
View Journal | View Issue

Cite this: *RSC Adv.*, 2021, **11**, 2040

A low temperature organic synthesis of monodispersed NiRu nanocrystals for CO_2 methanation†

Yang Liu,[ab] Xin Liang,[c] Jie Zhang,[c] Jimmy Yun[de] and Zuobo Yang *[c]

Received 8th October 2020
Accepted 23rd November 2020

DOI: 10.1039/d0ra08562f

rsc.li/rsc-advances

In this study, monodispersed NiRu nanocrystals with a diameter of 3 nm were synthesized at 90 °C *via* a tuning hot-inject method to lower the temperature of the organic phase synthesis of monodispersed nanomaterials. The key factor for the nanocrystalline formation of NiRu alloy nanocrystals was summarized in detail. Simultaneously, the synergistic effect of Ni and Ru in CO_2 methanation was explored. Doping trace Ru can significantly improve the conversion rate of CO_2 methanation and CH_4 selectivity. The underlying mechanism was studied in detail *via* X-ray diffraction (XRD), X-ray photoelectron spectroscopy (XPS), temperature-programmed hydrogen reduction (H_2-TPR) and desorption (H_2-TPD) tests, and temperature-programmed desorption of CO_2 (CO_2-TPD). This study gives out a new way for the general synthesis of monodisperse nickel-based nanocrystals and provides a reference for the development and application of monodispersed nanoparticles for CO_2 methanation.

1. Introduction

Carbon dioxide (CO_2) is a well-known greenhouse gas, which has led to a global climate change.[9–12] CO_2 capture and recovery is an effective method to deal with the increasing greenhouse effect.[13–15] CO_2 methanation for producing hydrocarbons is one of the effective ways of converting waste into resources and energy to solve the problem of CO_2 emissions caused by environmental and energy crisis.[16–20] Besides, CO_2 methanation could be a good route for hydrogen storage and transportation, which could make full use of green hydrogen produced by renewable energy, such as solar energy or by industrial water gas reaction,[9,21,22] contributing to the further realization of a low-carbon society in the future. A lot of research has already been done on CO_2 methanation using supported nickel-based catalysts due to their low cost and easy availability.[9,17,18,23–27] The addition of a second metal is an effective way to enhance the stability and catalytic activity of the nickel-based catalysts. Ruthenium is identified as more active in CO_x methanation, providing a larger range of catalytic reaction temperature compared to nickel, but is also considerably more expensive. Thus, it is necessary to investigate the CO_2 methanation performance of NiRu bimetallic nanocatalysts, which is likely to obtain better catalytic activity.

In the traditional catalyst preparation system, due to the limitations of synthetic methods and technologies, catalysts have numerous complex and diverse interfacial forms. For example, the existence of different grain sizes and complex surface morphology of the carrier makes it difficult to create a single regulatory variable process in the catalyst development, which is not conducive to establish the relationship between the microscopic size and the catalytic reaction at the mechanism level. The monodispersed nanoparticles can well solve this problem. The bulk-building material of monodispersed nanoparticles (generally sub-10 nm in size) with highly structured morphology and concentrated size distribution provides an ideal basis for studying catalytic reactions. In the traditional monodispersed Ni-based bimetal composite magnetic nanoparticles, most of them are prepared using oleylamine and oleic acid surface adsorbents[1,2] *via* the high-temperature pyrolysis of precursors.[3,4] However, in this synthesis system, as the synthesis temperature is generally higher than 150 °C,[5,6] it is difficult to achieve large-scale and high yield preparation. Therefore, it is of great significance to develop the synthesis system of medium and low-temperature monodispersed nickel-based nanoparticles. In the monodisperse nickel-based nanoparticle synthesis system, the precursor used for pyrolysis usually from carbonyl compounds is expensive and made up of special complexes.[7] The high cost and high toxicity make it difficult to popularize this method. Therefore, it is necessary to explore synthesis methods for monodispersed nickel-based materials with a harmless and low-cost precursor. To prepare nickel-

[a]*Sinopec Research Institute of Safety Engineering, Qingdao, 266000, China*
[b]*Qingdao Nuocheng Chemical Safety Technology Co., Ltd, Qingdao, 266071, China*
[c]*State Key Laboratory of Chemical Resource Engineering, Beijing University of Chemical Technology, Beijing, 100029, China. E-mail: zuoboyang319@163.com*
[d]*Qingdao International Academician Park Research Institute, Qingdao, Shandong 266000, PR China*
[e]*School of Chemical Engineering, The University of New South Wales, Sydney, NSW 2052, Australia*

† Electronic supplementary information (ESI) available: Literature comparison. See DOI: 10.1039/d0ra08562f

based monodisperse alloy nanoparticles, it is necessary to overcome the difficulties of different reduction potentials of different precursors. With the traditional high-temperature pyrolysis method, it is difficult to prepare alloy nanoparticles with uniform distribution of elements, but it is easier to form core–shell structures.[8]

As a result, a tuning hot-inject method was improved in order to reduce the temperature of the organic phase synthesis of monodispersed NiRu nanocrystals. The mechanism is shown in Scheme 1. $NaBH_4$ was introduced to achieve the co-reduction of Ni and Ru rather than *via* the pyrolysis of organometallic precursors method at a high temperature (>150 °C). DMF was introduced to serve as a solvent for $NaBH_4$ due to the limited solubility of $NaBH_4$ in oleylamine. As a result, when injecting the DMF solution of $NaBH_4$ into the oleylamine solution of $Ni(acac)_2$ and $RuCl_3$, $NaBH_4$ will quickly diffuse into the oleylamine solvent owing to the excellent solubility of DMF. With the release of hydrogen protons, Ni and Ru atoms are rapidly reduced and enter the process of common nucleus detonation. After that, the co-nucleated NiRu NPs will be covered by oleylamine molecules that inhibit the agglomeration of nanoparticles at the nuclear growth stage.

In summary, Ni and Ru achieve the simultaneous reduction despite their high reducing potential difference because of the high reducing properties of $NaBH_4$ in our proposed synthetic system. Monodispersed NiRu alloy nanoparticles with uniform elemental and particle size distributions were obtained and loaded onto an Al_2O_3 support as an ideal-building bulk material for CO_2 methanation.[28,29] The NiRu/Al_2O_3 catalysts show enhanced performance than that reported in the existing literature (Table S1†) and exhibit obvious synergistic effects.

2. Experimental

2.1 Materials

All chemicals were used as-received without any further purification: nickel(II) acetylacetonate (Ni (acac)$_2$, 95%, Aladdin), oleylamine ($C_{18}H_{37}N$, 80–90%, Aladdin), ruthenium(III) chloride anhydrous ($RuCl_3$, 45–55% Ru content, Aladdin), *N*,*N*-dimethylformamide (DMF, 99.5%, Sinopharm Chemical Reagent), ethanol (C_2H_6O, ≥99.5%, Aladdin), cyclohexane (C_6H_{12}, 99.9%, Sinopharm Chemical Reagent), acetone (C_6H_{12}, 99.9%, Sinopharm Chemical Reagent).

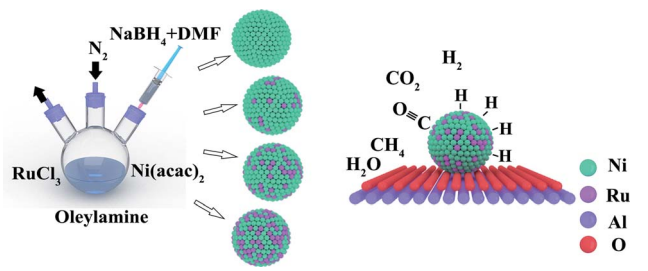

Scheme 1 Schematic of the preparation procedure of monodispersed NiRu NPs for CO_2 methanation.

2.2 Preparation of NiRu NPs

NiRu NPs (Ni/Ru atomic ratio of Ni_1Ru_0, $Ni_{0.95}Ru_{0.05}$, $Ni_{0.9}Ni_{0.1}$, $Ni_{0.8}Ru_{0.2}$ = 10 : 0, 9.5 : 0.5, 9 : 1, 8 : 2) were prepared by a tuning hot-inject method. Taking $Ni_{0.9}Ni_{0.1}$ NPs as an example, 0.9 mmol $Ni(acac)_2$ and 0.1 mmol $RuCl_3$ were dissolved in 15 mL oleylamine and transferred into a 50 mL three-necked flask, and then heated in an oil bath at 90 °C under N_2 atmosphere for 1 h. 100 mg $NaBH_4$ dissolved in 2 mL DMF was pre-heated in a 70 °C oven for 10 min was injected into the above solution. Numerous bubbles were released and the solution turned black immediately. After 1 h, the three-mouth flask was lifted from the oil bath and cooled to room temperature. After that, cyclohexane and acetone were added to the product solution and centrifuged for washing. The process was repeated five times to remove oleylamine as far as possible from the surface, and black solid particles were obtained. Finally, the colloidal particles were dissolved in 10 mL cyclohexane for further use. To explore the influence of temperature. Ni_1Ru_0 nanocrystals were synthesized at 80 °C, 90 °C, 100 °C, and 110 °C, respectively, as an example.

2.3 Preparation of 10 wt% NiRu/Al_2O_3

γ-Al_2O_3 was synthesized by the hydrothermal synthesis method based on the reported literature.[30] 60 mL H_2O, 7.5 g aluminum nitrate and 6 g urea were transformed into a 100 mL Teflon-lined stainless-steel autoclave, which was sealed and maintained at 120 °C for 24 h. After cooling to room temperature, the samples were washed 3 times and dried for 6 h in an air atmosphere of 70 °C. The dried samples were calcined at 550 °C for 6 h, and the temperature was lowered to room temperature to obtain a final willow leaf-like γ-Al_2O_3 product for further use. γ-Al_2O_3 was dispersed in 40 mL cyclohexane and stirred evenly *via* ultrasonication. Then, 10 mL of the $Ni_xRu_{(1-x)}$ cyclohexane solution obtained in the previous experimental step was poured into the solution. A uniform brown color was obtained, and the solution was ultrasonically stirred for 2 h. After standing for 30 min, the solution was separated into two layers. The upper layer was transparent cyclohexane, and the lower layer was loaded with $Ni_xRu_{(1-x)}$/γ-Al_2O_3 flocculation, indicating that the $Ni_xRu_{(1-x)}$ colloid particles that were originally soluble in cyclohexane were completely loaded onto the γ-Al_2O_3 carrier. After the loading was completed, the suspension was centrifuged once again at a low rotation speed (8000 rpm, 3 min), dried in a 70 °C oven for 4 h.

2.4 Catalytic experiments

CO_2 methanation catalytic activity was evaluated in an 8 mm fixed-bed steel tube microreactor at atmospheric pressure. 0.1 g catalyst powder was mixed with 0.2 g quartz sand (60–70 mesh sieved) and then reduced at 350 °C for 2 h in 25 mL min^{-1} H_2 flow before the run. Next, the sample was cooled from 350 to 200 °C. Following the catalyst pre-treatment, the reactant gas containing 15% CO_2: 60% H_2: 25% N_2 was passed through the reactor bed at a total flow rate of 26.67 mL min^{-1} (WHSV of *ca.* 12 000 mL h^{-1} g^{-1}). In order to explore the effects of Ru doping

on NiRu/Al_2O_3, the catalytic performance of the NiRu/Al_2O_3 catalyst with Ru contents of 0%, 5%, 10%, and 20% were investigated under the condition of 200–400 °C temperature at atmospheric pressure (each sampling temperature point was stable for 1 h to obtain a relatively stable data). Product analysis was performed with Varian CP-3800 chromatography equipped with a TCD detector.

2.5 Characterization

Transmission Electron Microscopy (TEM) was carried out on a Hitachi HT7700 with an accelerating voltage of 120 kV (10 microliters of NiRu NPs in cyclohexane solution were dropped onto the carbon support film and dried at room temperature). The crystallinity of catalysts was determined by X-ray diffraction (XRD) using X'Pert Pro (Cu Kα radiation, 40 kV, 30 mA, λ = 1.5418 Å). In the H_2-TPR method, 50 mg of the samples were heated from 50 to 600 °C (10 °C min^{-1} heating rate, 30 mL min^{-1} 5% H_2/N_2). Before the TPR measurement, each sample was flushed with He flow at 200 °C for 60 min and cooled to 30 °C. In the H_2-TPD method, 50 mg of the samples were pretreated at 350 °C under 5% H_2/He for 2 h, purged with He for 0.5 h, and then cooled to 50 °C to adsorb H_2 (50 m min^{-1}, 40 min). After they were purged with He for 30 min, the samples were heated to 800 °C at a rate of 10 °C min^{-1}. In the CO_2-TPD method, 50 mg of the samples were reduced at 350 °C under 5% H_2/He for 30 min, treated with He flow at 350 °C for 15 min, and then cooled to 100 °C. CO_2 (50 mL min^{-1}) was adsorbed on the samples for 1 h at 100 °C and cooled to 50 °C. The temperature was then raised to 500 °C at a heating rate of 10 °C min^{-1} under He flow. N_2 adsorption and desorption isotherms were measured by an automatic physical adsorption analyzer (Micromeritics ASAP2020). The samples were degassed at 150 °C for 2 h to remove physically absorbed water and impurities on the surface before the measurement. The specific surface area was calculated by the Brunauer–Emmett–Teller (BET) method and pore size distribution was analyzed by the Barrett–Joyner–Halenda (BJH) method. XPS spectra of the catalysts were obtained using a KRATOS AXIS-NOVA (Shimadzu Corporation) instrument with a monochromatic Al-Kα as an X-ray source. The binding energy shift caused by the relative surface charging was corrected using the C 1s level as an internal standard. ICP-OES was performed to analyse the metal content of NiRu/Al_2O_3 catalysts.

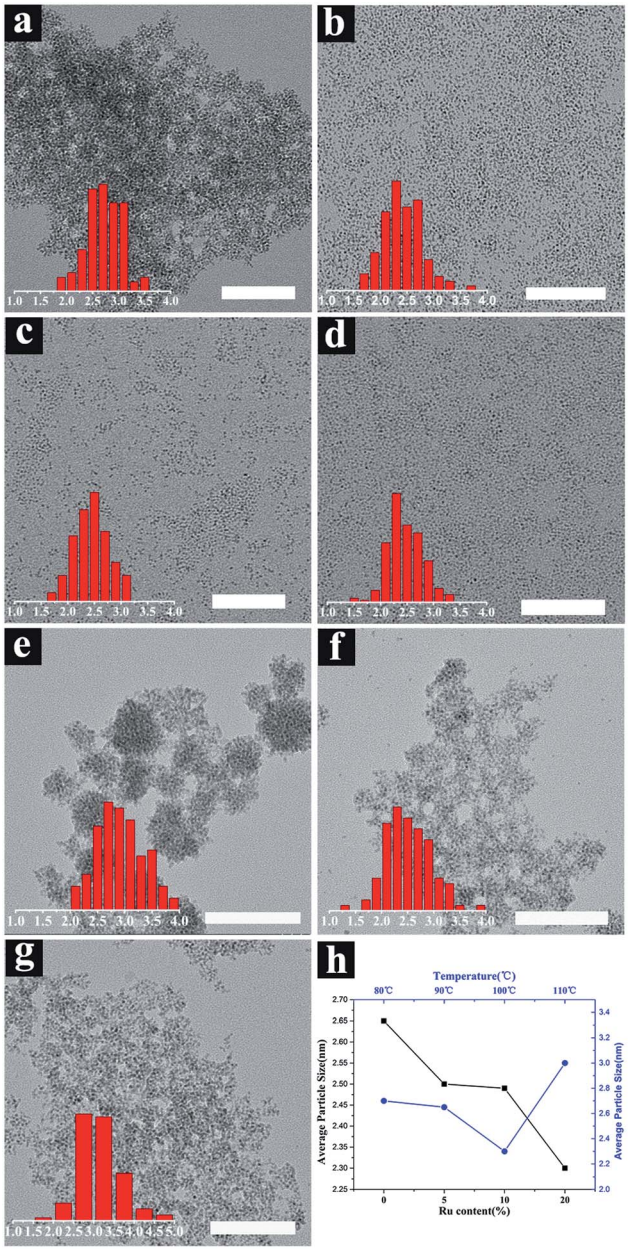

Fig. 1 TEM results of (a–d) Ni_1Ru_0, $Ni_{0.95}Ru_{0.05}$, $Ni_{0.9}Ru_{0.1}$ and $Ni_{0.8}Ru_{0.2}$ nanoparticles at a synthetic temperature of 90 °C (scan bar: 100 nm). (d–g) Ni_1Ru_0 nanoparticles at synthesis temperatures of 80, 100 and 110 °C. (h) Particle size of Ni_1Ru_0 nanoparticles at different synthesis temperatures.

3. Results and discussion

3.1 Standard characterization

3.1.1 TEM analysis. As shown in Fig. 1 a–d, the monodisperse $Ni_xRu_{(1-x)}$ with different Ru doping contents was successfully synthesized, and the particle diameter was about 2.5 nm. In contrast, Ni_1Ru_0 shows a bigger particle size than others and is easier to agglomerate according to the TEM results; while Ru doping in the synthesis process reduces the diameter of the size of the nanoparticles (Fig. 1h) and significantly improves the dispersion and uniformity of nanocrystals. The experimental results showed that after the introduction of Ru, the generation rate of hydrogen improved when the DMF solution containing $NaBH_4$ was injected into the oleylamine solution containing the NiRu precursor. This indicates that the introduction of Ru was likely to promote the decomposition of $NaBH_4$ and accelerate the release of reducing hydrogen protons, then promoting the nucleation process and thus leading to a more concentrated nanometer size of $Ni_xRu_{(1-x)}$ doped by Ru. This synthesis system covers a wide temperature window. To investigate the influence of temperature during the synthesis process of NiRu nanoparticles, Ni_1Ru_0 nanocrystals were

synthesized at different temperatures ranging from 80 to 110 °C. According to the TEM results (Fig. 1e–h), the agglomeration of nickel nanoparticles was more severe at low temperature (80 °C). The diameter of nanoparticles decreases from 2.7 nm to 2.3 nm with the increase in the synthesis temperature (80–100 °C), but the particle size increased to 3 nm when the synthesis temperature was 110 °C. The reason is that temperature rising (below 100 °C) can increase the diffusion rate of $NaBH_4$ at DMF and promote the release of hydrogen protons, which increased the nucleation concentration leading to a smaller nanoparticle diameter. However, when the temperature is above 100 °C, Ostwald ripening will be the rate determining step for the diameter of the nanoparticles.

3.1.2 XRD analysis. X-ray diffraction (XRD) patterns of NiRu NPs are shown in Fig. 2a. Ni_1Ru_0, $Ni_{0.95}Ru_{0.05}$, $Ni_{0.9}Ru_{0.1}$ and $Ni_{0.8}Ru_{0.2}$ all show characteristic peaks of Ni (JCPDS 47-1049) and NiO (JCPDS 4-0850), but no characteristic peaks of Ru. It indicated that NiRu nanocrystals exhibit the nickel crystal structure. Among them, Ni_1Ru_0 and $Ni_{0.95}Ru_{0.05}$ showed significant NiO diffraction peaks at positions 37°, 43° and 63°, which should be caused by the oxidation of Ni on the surface of Ni_1Ru_0 and $Ni_{0.95}Ru_{0.05}$ by oxygen present in the air during the drying process. In contrast, $Ni_{0.9}Ru_{0.1}$ and $Ni_{0.8}Ru_{0.2}$ showed almost pure Ni characteristic peaks with no diffraction peaks of NiO. XRD results of $NiRu/Al_2O_3$ are shown in Fig. 2b; only a weak diffraction peak of the Al_2O_3 support can be observed due to the very small particle size of NiRu NPs. The XRD patterns of $NiRu/Al_2O_3$ after H_2 reduction showed almost the same peak position and intensity compared with $NiRu/Al_2O_3$ even after the catalytic performance evaluation, indicating that there were no crystal changes during the CO_2 methanation process. Ni_1Ru_0/Al_2O_3 showed an obvious face-centered cubic (hcp) Ni crystal structure (JCPDS no. 45-1027). The intensity of the Ni diffraction peak decreases with the increase in the ruthenium introduction, which might be because Ru doping could inhibit the NiRu nanocrystal growth under high-temperature CO_2 methanation conditions.

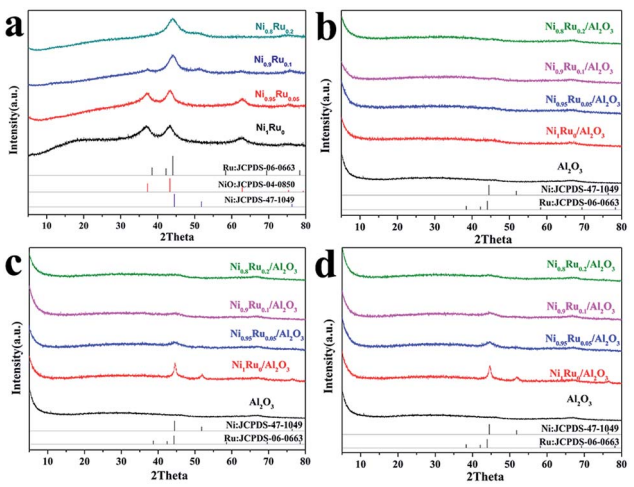

Fig. 2 XRD results of (a) NiRu NPs with Ar treatment at 300 °C, (b) $NiRu/Al_2O_3$, (c and d) $NiRu/Al_2O_3$ after H_2 reduction and after the catalytic performance test.

3.2 CO_2 methanation catalytic activity study

Fig. 3 shows CO_2 conversion and CH_4 selectivity of $NiRu/Al_2O_3$ catalysts as a function of the reaction temperature. All of the $NiRu/Al_2O_3$ shows better performance than Ni/Al_2O_3 catalysts. The CH_4 selectivity was significantly improved for $NiRu/Al_2O_3$ with almost 100% CH_4 selectivity, particularly at low temperature (<350 °C) compared with that for Ni/Al_2O_3. $Ni_{0.9}Ru_{0.1}/Al_2O_3$ and $Ni_{0.95}Ru_{0.05}/Al_2O_3$ showed almost similar CO_2 conversion and CH_4 selectivity when the temperature was below 300 °C. $Ni_{0.9}Ru_{0.1}/Al_2O_3$ shows better performance at 325 °C and achieves the highest CO_2 conversion (89.7%) at 350 °C, superior to that of most reported nickel-based CO_2 methanation catalysts (Table S1†). Comparative tests were conducted to illustrate the key role of the DMF solvent for $NaBH_4$ and the effect of the low solubility of $NaBH_4$ in oleylamine. DMF and 1 : 1 volume ratio DMF : oleylamine were two contrasting solvents for $NaBH_4$. $NaBH_4$ completely dissolved in DMF. By contrast, some crystals precipitated and could be observed in the oleylamine and DMF solvent mixture. According to the catalytic performances of the catalysts synthesized under two different solvents for $NaBH_4$, as

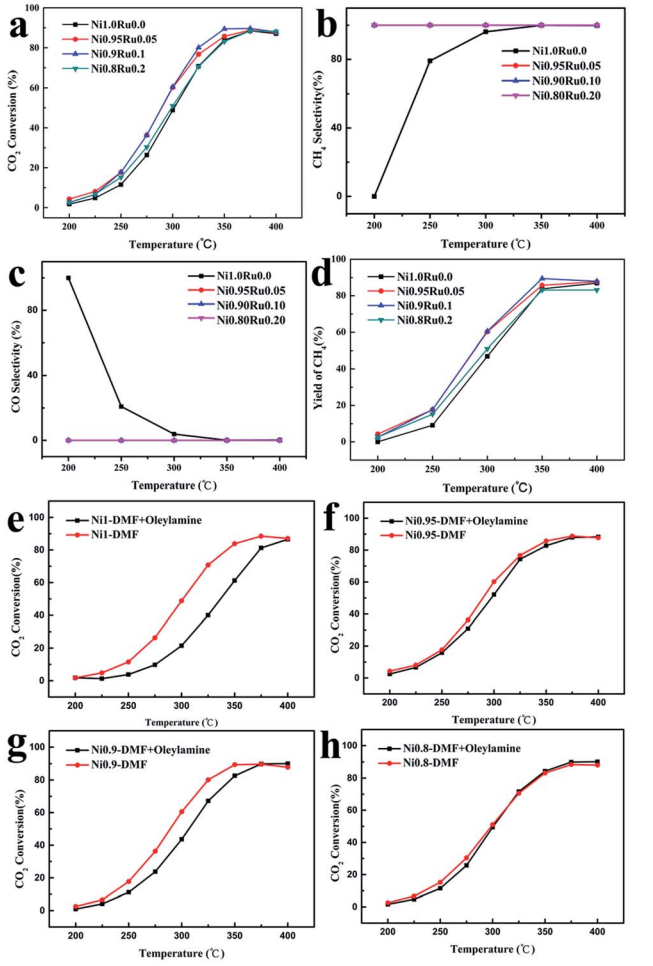

Fig. 3 (a) CO_2 conversion rate curve, (b) CH_4 selectivity curve, (c) CO selectivity curve, (d) CH_4 yield curve of $NiRu/Al_2O_3$ at different temperatures. (e–h) The catalytic performance of CO_2 methanation $Ni_xRu_{(1-x)}/\gamma\text{-}Al_2O_3$ prepared with different solutions of $NaBH_4$.

shown in Fig. 3 a–d, $NiRu/Al_2O_3$ with DMF as a solvent for $NaBH_4$ showed better performance than that prepared in the oleylamine and DMF solvent mixture. Therefore, DMF plays a crucial role in this synthesis system. When the DMF solution of $NaBH_4$ was injected into the oleylamine solution of $Ni(acac)_2$ and $RuCl_3$, the DMF solution of $NaBH_4$ would rapidly diffuse into the oleylamine solvent and rapidly dissolve. Therefore, $NaBH_4$ was decomposed and $Ni(acac)_2$ and $RuCl_3$ were reduced before their precipitation. After that, NiRu NPs were coated by oleylamine and entered the nuclear growth stage. Finally, the monodispersed NiRu alloy NPs were obtained.

3.3 TPR, TPD, N_2 adsorption and desorption isotherms, XPS analyses

H_2-TPR, H_2-TPD, CO_2-TPD, BET characterization and XPS studies were carried out to study the reasons for the improved performance of CO_2 methanation on $Ni_{0.9}Ru_{0.1}/Al_2O_3$ compared with Ni/Al_2O_3. Fig. 4a shows the H_2-TPR profiles of Ni_1Ru_0/Al_2O_3 and $Ni_{0.9}Ru_{0.1}/Al_2O_3$, it can be observed that there were three main peaks centered at 144–205 °C (peak A), 205–284 °C (peak B) and 284–387 °C (peak C) for $Ni_{0.9}Ru_{0.1}/Al_2O_3$. In contrast, only two main peaks centered at 123–192 °C (peak D), 200–346 °C (peak E) and a weak peak centered at 73.6 °C were detected for Ni_1Ru_0/Al_2O_3. According to the H_2-TPR results, the peak located at 73.6 °C should be attributed to oxygen adsorption on the surface of Ni NPs or the surface of NiO, and peaks A and D should be attributed to $NiRuO_x$ strongly interacting with Al_2O_3.[31] It matched with the XRD results (Ni_1Ru_0 can be easily oxidized under the air condition). Peak C and F are attributed to the subsurface oxygens of Al_2O_3. It is worth noting that $Ni_{0.9}Ru_{0.1}/Al_2O_3$ has an extra peak B. We believe that the peak B should be attributed to the weakly interacting $NiRuO_x$ and the H-spillover effects. For $Ni_{0.9}Ru_{0.1}/Al_2O_3$, the NiRu site is tightly bound to Al_2O_3 and will be reduced first, and the weakly interacting $NiRuO_x$ will then be reduced. After that, the hydrogen overflow happens on the reduced NiRu surface and reacted with the subsurface oxygens. It can explain why the area of peak C is smaller than that of peak E, and consistent with the H_2-TPD results ($Ni_{0.9}Ru_{0.1}/Al_2O_3$ shows higher temperature location of hydrogen desorption peaks at 443.9 °C compared to the 437.3 °C peak of Ni_1Ru_0/Al_2O_3). The hydrogen desorption quality was calculated from the areas of the corresponding desorption peaks. $Ni_{0.9}Ru_{0.1}/Al_2O_3$ showed a higher H_2 desorption quantity (21.795 $cm^3\ g^{-1}$) compared to that by Ni_1Ru_0/Al_2O_3 (7.636 $cm^3\ g^{-1}$), which indicates that $Ni_{0.9}Ru_{0.1}/Al_2O_3$ has stronger hydrogen adsorption capability than Ni_1Ru_0/Al_2O_3. Fig. 4c shows the CO_2-TPD profile of Ni_1Ru_0/Al_2O_3 and $Ni_{0.9}Ru_{0.1}/Al_2O_3$. $Ni_{0.9}Ru_{0.1}/Al_2O_3$ shows a huge distinctive CO_2-TPD peak compared with Ni_1Ru_0/Al_2O_3. Two desorption peaks at 200–350 °C and 350–450 °C can be observed for Ni_1Ru_0/Al_2O_3 that correspond to weak basic sites and medium-strength basic sites. In contrast, only one desorption peak at 350–500 °C, corresponding to medium-strength basic sites was detected for Ni_1Ru_0/Al_2O_3. In CO_2 methanation reactions, medium-strength basic sites are more active than the weak basic site. $Ni_{0.9}Ru_{0.1}/Al_2O_3$ also showed higher CO_2 desorption quantity (1068 $cm^3\ g^{-1}$) than Ni_1Ru_0/Al_2O_3 (405 $cm^3\ g^{-1}$), which indicated that $Ni_{0.9}Ru_{0.1}/Al_2O_3$ has better CO_2 chemisorption than that by Ni_1Ru_0/Al_2O_3. Ni_1Ru_0/Al_2O_3 and $Ni_{0.9}Ru_{0.1}/Al_2O_3$ show similar N_2 adsorption and desorption isotherms displaying the IV type isotherms with an apparent hysteresis loop according to the IUPAC classification, the type H_2 hysteresis loop appears in the region of $0.4–0.7 p/p_o$, indicating a narrow mesopore size distribution. In addition to the high specific surface area, $Ni_{0.9}Ru_{0.1}/Al_2O_3$ shows approximately the same physical parameters compared with Ni_1Ru_0/Al_2O_3; therefore, the synergistic effects is the core factor affecting the catalytic performance (Table 1). XPS characterization was performed to acquire more information on the surface species of the catalysts that completed the CO_2 methanation activity test. In the Ni 2p XPS spectra (Fig. 4f), the peaks located at 855.6, 873.6 eV can be assigned to Ni^{2+} $2p_{3/2}$ and $2p_{1/2}$, respectively, and the peak at 852.5 eV belongs to Ni^0. Compared to Ni_1Ru_0/Al_2O_3, the Ni $2p_{3/2}$ peak of Ni^{2+} largely increased for $Ni_{0.9}Ru_{0.1}/Al_2O_3$.

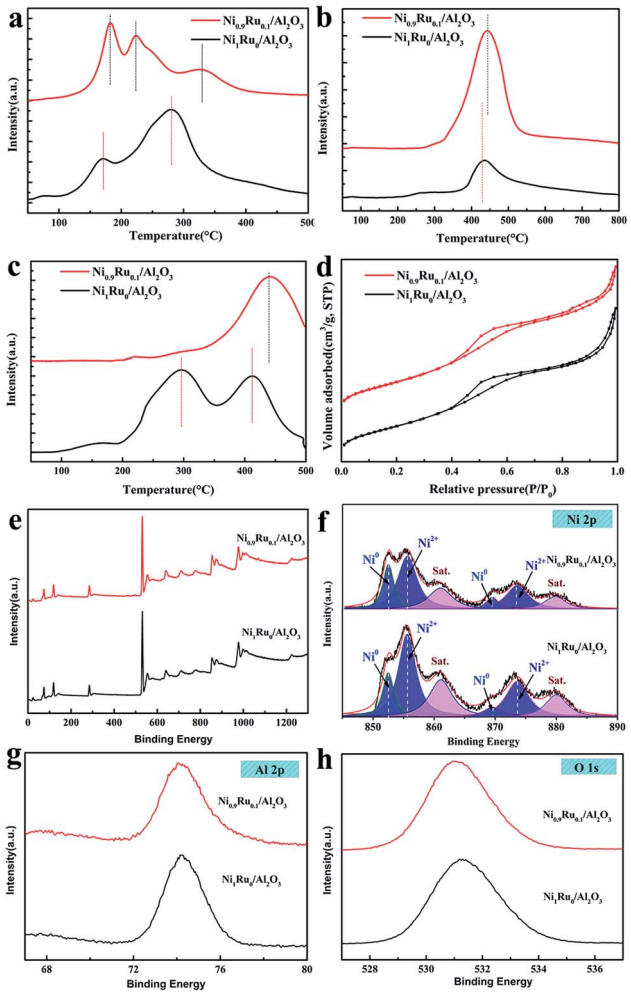

Fig. 4 (a) H_2-TPR, (b) H_2-TPD, (c) CO_2-TPD profile of $NiRu/Al_2O_3$, (d) N_2 adsorption–desorption isotherms of $NiRu/Al_2O_3$. (e) Survey scan. (f) High-resolution Ni 2p spectra. (g) High-resolution Al 2p spectra. (h) High-resolution O 1s spectra.

Table 1 Physical properties of Ni_1Ru_0/Al_2O_3 and $Ni_{0.9}Ru_{0.1}/Al_2O_3$

Catalyst	Ni_1Ru_0/Al_2O_3	$Ni_{0.9}Ru_{0.1}/Al_2O_3$
S_{BET}[a]/(m^2 g^{-1})	336.2	360.9
V_p[b] (m^3 g^{-1})	0.575	0.576
D_p[c] (nm)	3.38	3.38
Ni[d] (wt%)	9.95	8.96
Ru[d] (wt%)	0	1.003

[a] Calculated from the BET equation. [b] BJH desorption pore volume. [c] BJH desorption average pore diameter. [d] Calculated from ICP-OES results.

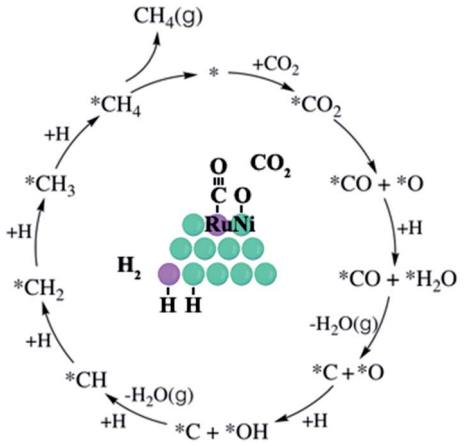

Fig. 5 CO_2 methanation scheme on $NiRu/Al_2O_3$.

3.4 CO_2 methanation scheme of $NiRu/Al_2O_3$

The possible pathways for CO_2 methanation are summarized in Fig. S1,† and the kinetics reaction of CO_2 methanation was found to follow the direct C–O bond cleavage pathway (Fig. 5) for $Ni/\gamma\text{-}Al_2O_3$ catalysts, in which the rate-limiting step was the subsequent dissociation of adsorbed *CO.[33] Surface metallic Ni can be oxidized by CO_2,[32] and we believe that the Ru site easily absorbs CO and neighbouring Ni site adsorbs dissociated O during the CO_2 decompose process for the NiRu crystal surface. It can be supported from CO_2 TPD s and XPS results (more Ni^{2+} content). Alternatively, Ru doping promotes the CO_2 decomposition, which leads to improved CO_2 methanation activity. On the other hand, the rate-limiting step for CO production through the reverse water gas shift reaction was identified as *CO desorption.[34] Ru has a stronger adsorption capacity to *CO, which inhibits the desorption of the *CO, leading to enhanced CH_4 selectivity for the $NiRu/Al_2O_3$ catalyst. In summary, the addition of Ru promotes the dissociation of carbon dioxide and inhibits the formation of CO. The acceleration of dissociated hydrogen species promotes the production of methane and finally makes the catalyst show a better catalytic performance of the methanation.

4. Conclusions

The monodispersed NiRu nanocrystals were prepared at a low temperature by modified heat injection with $NaBH_4$ as the reducing agent and loaded onto Al_2O_3 to be an ideal building block for CO_2 methanation. Affected by the compositional effect, $Ni_{0.9}Ru_{0.1}/Al_2O_3$ exhibits the best performance for both CO_2 conversion and CH_4 selectivity. The underlying mechanism was carefully studied by XRD, ICP, H_2-TPR, H_2-TPD, CO_2-TPD, BET, and XPS. All the characterization results indicate that Ru doping is an effective means to improve the performance of the Ni-based CO_2 methanation catalyst, which could promote hydrogen adsorption, desorption and H-spillover effects, and promote CO_2 chemisorption. This work has put forward a new strategy for the synthesis of monodispersed nickel-based nanocrystals and provides a fresh idea for the development and application of precious metals in nickel-based catalysts for CO_2 methanation.

Conflicts of interest

There are no conflicts to declare.

Acknowledgements

This work was financially supported by National Natural Science Foundation of China (NSFC) (General Program No. 21571012).

Notes and references

1 O. Metin, V. Mazumder, S. Ozkar and S. Sun, Monodisperse nickel nanoparticles and their catalysis in hydrolytic dehydrogenation of ammonia borane, *J. Am. Chem. Soc.*, 2010, **132**(5), 1468–1469.
2 A. P. LaGrow, B. Ingham, S. Cheong, G. V. M. Williams, C. Dotzler, M. F. Toney, D. A. Jefferson, E. C. Corbos, P. T. Bishop, J. Cookson and R. D. Tilley, Synthesis, Alignment, and Magnetic Properties of Monodisperse Nickel Nanocubes, *J. Am. Chem. Soc.*, 2012, **134**(2), 855–858.
3 Q. Li and S. Sun, Recent advances in the organic solution phase synthesis of metal nanoparticles and their electrocatalysis for energy conversion reactions, *Nano Energy*, 2016, **29**, 178–197.
4 A. P. LaGrow, B. Ingham, M. F. Toney and R. D. Tilley, Effect of Surfactant Concentration and Aggregation on the Growth Kinetics of Nickel Nanoparticles, *J. Phys. Chem. C*, 2013, **117**(32), 16709–16718.
5 M. Shviro and D. Zitoun, Tip Enhanced Silver Growth on Shaped Controlled Nickel Nanocrystals, *J. Phys. Chem. C*, 2014, **118**(19), 10455–10462.
6 K. E. Marusak, A. C. Johnston-Peck, W.-C. Wu, B. D. Anderson and J. B. Tracy, Size and Composition Control of CoNi Nanoparticles and Their Conversion into Phosphides, *Chem. Mater.*, 2017, **29**(7), 2739–2747.
7 M. Heilmann, H. Kulla, C. Prinz, R. Bienert, U. Reinholz, A. Guilherme Buzanich and F. Emmerling, Advances in Nickel Nanoparticle Synthesis *via* Oleylamine Route, *Nanomaterials*, 2020, **10**(4), 713.
8 H. Lv, Z. Xi, Z. Chen, S. Guo, Y. Yu, W. Zhu, Q. Li, X. Zhang, M. Pan, G. Lu, S. Mu and S. Sun, A New Core/Shell NiAu/Au

Nanoparticle Catalyst with Pt-like Activity for Hydrogen Evolution Reaction, *J. Am. Chem. Soc.*, 2015, **137**(18), 5859–5862.

9 M. Cai, J. Wen, W. Chu, X. Cheng and Z. Li, Methanation of carbon dioxide on Ni/ZrO_2-Al_2O_3 catalysts: effects of ZrO_2 promoter and preparation method of novel ZrO_2-Al_2O_3 carrier, *J. Nat. Gas Chem.*, 2011, **20**(3), 318–324.

10 H. Liu, X. Zou, X. Wang, X. Lu and W. Ding, Effect of CeO_2 addition on Ni/Al_2O_3 catalysts for methanation of carbon dioxide with hydrogen, *J. Nat. Gas Chem.*, 2012, **21**(6), 703–707.

11 T. A. Le, J. Kim, Y. R. Jeong and E. D. Park, CO_2 Methanation over $Ni/Al@MAl_2O_4$ (M = Zn, Mg, or Mn) Catalysts, *Catalysts*, 2019, **9**(7), 599.

12 Z.-H. Huang, F.-F. Sun, M. Batmunkh, W.-H. Li, H. Li, Y. Sun, Q. Zhao, X. Liu and T.-Y. Ma, Zinc–nickel–cobalt ternary hydroxide nanoarrays for high-performance supercapacitors, *J. Mater. Chem. A*, 2019, **7**(19), 11826–11835.

13 A. Beuls, C. Swalus, M. Jacquemin, G. Heyen, A. Karelovic and P. Ruiz, Methanation of CO_2: further insight into the mechanism over Rh/γ-Al_2O_3 catalyst, *Appl. Catal., B*, 2012, **113–114**, 2–10.

14 E. H. Cho, W. Kim, C. H. Ko and W. L. Yoon, Enhanced CO_2 Methanation Reaction in C_1 Chemistry over a Highly Dispersed Nickel Nanocatalyst Prepared Using the One-Step Melt-Infiltration Method, *Catalysts*, 2020, **10**(6), 643.

15 J. B. Branco, R. P. da Silva and A. C. Ferreira, Methanation of CO_2 over Cobalt-Lanthanide Aerogels: Effect of Calcination Temperature, *Catalysts*, 2020, **10**(6), 704.

16 T. Sakakura, J.-C. Choi and H. Yasuda, Transformation of Carbon Dioxide, *Chem. Rev.*, 2007, **107**(6), 2365–2387.

17 I. Rossetti, C. Biffi, C. L. Bianchi, V. Nichele, M. Signoretto, F. Menegazzo, E. Finocchio, G. Ramis and A. Di Michele, Ni/SiO_2 and Ni/ZrO_2 catalysts for the steam reforming of ethanol, *Appl. Catal., B*, 2012, **117–118**, 384–396.

18 H. C. Wu, Y. C. Chang, J. H. Wu, J. H. Lin, I. K. Lin and C. S. Chen, Methanation of CO_2 and reverse water gas shift reactions on Ni/SiO_2 catalysts: the influence of particle size on selectivity and reaction pathway, *Catal. Sci. Technol.*, 2015, **5**(8), 4154–4163.

19 S. Tada, T. Shimizu, H. Kameyama, T. Haneda and R. Kikuchi, Ni/CeO_2 catalysts with high CO_2 methanation activity and high CH_4 selectivity at low temperatures, *Int. J. Hydrogen Energy*, 2012, **37**(7), 5527–5531.

20 Y. Guo, S. Mei, K. Yuan, D.-J. Wang, H.-C. Liu, C.-H. Yan and Y.-W. Zhang, Low-Temperature CO_2 Methanation over CeO_2-Supported Ru Single Atoms, Nanoclusters, and Nanoparticles Competitively Tuned by Strong Metal–Support Interactions and H-Spillover Effect, *ACS Catal.*, 2018, **8**(7), 6203–6215.

21 Q. Zhang, Z. Yang, B. Chen and X. Liang, Phase-competition-driven formation of hierarchical FeNiZn-MIL-88B-on-MOF-5 octapods displaying high selectivity for the RWGS reaction, *Chem. Commun.*, 2019, **55**(58), 8450–8453.

22 R.-P. Ye, Q. Li, W. Gong, T. Wang, J. J. Razink, L. Lin, Y.-Y. Qin, Z. Zhou, H. Adidharma, J. Tang, A. G. Russell, M. Fan and Y.-G. Yao, High-performance of nanostructured Ni/CeO_2 catalyst on CO_2 methanation, *Appl. Catal., B*, 2020, **268**, 118474.

23 G. Du, S. Lim, Y. Yang, C. Wang, L. Pfefferle and G. L. Haller, Methanation of carbon dioxide on Ni-incorporated MCM-41 catalysts: the influence of catalyst pretreatment and study of steady-state reaction, *J. Catal.*, 2007, **249**(2), 370–379.

24 G. Garbarino, P. Riani, L. Magistri and G. Busca, A study of the methanation of carbon dioxide on Ni/Al_2O_3 catalysts at atmospheric pressure, *Int. J. Hydrogen Energy*, 2014, **39**(22), 11557–11565.

25 Z. Li, B. Li, Z. Li and X. Rong, The promoter action of CeO_2 for the Ni/Al_2O_3-catalyzed methanation of CO_2, *Kinet. Catal.*, 2015, **56**(3), 329–334.

26 V. Shanmugam, S. Neuberg, R. Zapf, H. Pennemann and G. Kolb, Effect of Support and Chelating Ligand on the Synthesis of Ni Catalysts with High Activity and Stability for CO_2 Methanation, *Catalysts*, 2020, **10**(5), 493.

27 L. Wang, J. Hu, H. Liu, Q. Wei, D. Gong, L. Mo, H. Tao and C. Zhang, Three-Dimensional Mesoporous Ni–CeO_2 Catalysts with Ni Embedded in the Pore Walls for CO_2 Methanation, *Catalysts*, 2020, **10**(5), 523.

28 H. Nagase, R. Naito, S. Tada, R. Kikuchi, K. Fujiwara, M. Nishijima and T. Honma, Ru nanoparticles supported on amorphous ZrO_2 for CO_2 methanation, *Catal. Sci. Technol.*, 2020, **10**(14), 4522–4531.

29 A. A. A. Mohammed, M. A. H. S. Saad, A. Kumar and M. J. Al-Marri, Synthesis of fumed silica supported Ni catalyst for carbon dioxide conversion to methane, *Greenhouse Gases: Sci. Technol.*, 2020, **10**(4), 715–724.

30 S. Liu, X. Liang, J. Zhang and B. Chen, Temperature sensitive synthesis of γ-Al_2O_3 support with different morphologies for $CoMo/\gamma$-Al_2O_3 catalysts for hydrodesulfurization of thiophene and 4,6-dimethyldibenzothiophene, *Catal. Sci. Technol.*, 2017, **7**(2), 466–480.

31 J. Lin, C. Ma, J. Luo, X. Kong, Y. Xu, G. Ma, J. Wang, C. Zhang, Z. Li and M. Ding, Preparation of Ni based mesoporous Al_2O_3 catalyst with enhanced CO_2 methanation performance, *RSC Adv.*, 2019, **9**(15), 8684–8694.

32 C.-c. Yu, Y. Lu, X.-j. Ding and S.-k. Shen, Studies on Ni/Al_2O_3 catalyst for CO_2 reforming of CH_4 to synthesis gas—a combined research of TPD, TPPR and XPS, in *Studies in Surface Science and Catalysis*, ed. M. dePontes, R. L. Espinoza, C. P. Nicolaides, J. H.Scholtz and M. S. Scurrell, Elsevier, 1997, vol. 107, pp. 503–510.

33 S. Kattel, P. Liu and J. G. Chen, Tuning Selectivity of CO_2 Hydrogenation Reactions at the Metal/Oxide Interface, *J. Am. Chem. Soc.*, 2017, **139**(29), 9739–9754.

34 T. Avanesian, G. S. Gusmão and P. Christopher, Mechanism of CO_2 reduction by H_2 on Ru(0001) and general selectivity descriptors for late-transition metal catalysts, *J. Catal.*, 2016, **343**, 86–96.